Ultralow Friction of Carbonate Faults Caused by Thermal Decomposition

Raehee Han, *et al.*

Science **316**, 878 (2007);
DOI: 10.1126/science.1139763

Science (print ISSN 0036-8075; online ISSN 1095-9203) is published weekly, except the last week in December, by the American Association for the Advancement of Science, 1200 New York Avenue NW, Washington, DC 20005.

beaming resulted from a blunt (*18*) or asymmetric shock (*2*). The asymmetric shock could result from an interstellar magnetic field inclined in a particular direction (*19*, *20*). In a recent report (*3*), we showed that an interstellar magnetic field in the HDP could distort the termination shock in a direction that explains the TSPs streaming outward at V1.

Figure 2 shows that for B_{ISM} parallel to the HDP, the longitude of the MD point (the minimum radial distance of the termination shock to the Sun) is greater than the longitude of V1, so the TSPs will stream outward along the spiral field. In the heliospheric southern hemisphere the longitude of V2 is greater than that of the MD point of the shock, so the TSPs will stream inward toward V2, as is observed. However, for B_{ISM} parallel to the GAL, the MD in the northern hemisphere shifts to a smaller longitude than V1, so that the TSPs would stream inward toward V1, opposite to what is observed.

In this calculation we did not include the neutral hydrogen atoms that interact with the ionized component by charge exchange. Although the inclusion of the neutral atoms will tend to symmetrize the solution and quantitatively affect the degree of asymmetry, the general character of the asymmetry is expected to remain the same, with the plane of symmetry of the distorted heliopause determined by the plane of the local interstellar magnetic field (*21*, *22*). Thus, it would be expected that different orientations of the local interstellar magnetic field would result in the same qualitative differences in the predicted radio source locations and streaming directions of upstream ions as described here. On the basis of those differences, and assuming that the source of radio emission is the region where the field draped on the heliopause is perpendicular to the radial direction, we find from Voyager observations that the plane of the local interstellar magnetic field is not parallel to the GAL but is 60° to 90° from that plane (rotated clockwise from a view from the Sun). This suggests that the field orientation in the Local Interstellar Cloud differs from that of a larger-scale interstellar magnetic field thought to parallel the GAL.

References and Notes

1. R. B. Decker *et al.*, *Science* **309**, 2020 (2005).
2. E. C. Stone *et al.*, *Science* **309**, 2017 (2005).
3. M. Opher, E. C. Stone, P. C. Liewer, *Astrophys. J.* **640**, L71 (2006).
4. P. C. Frisch, in *Physics of the Outer Heliosphere: Proceedings of the 1st COSPAR Colloquium* (Pergamon, Oxford, UK, 1990), pp. 19–28.
5. P. C. Frisch, *Space Sci. Rev.* **78**, 213 (1996).
6. R. Lallement *et al.*, *Science* **307**, 1447 (2005).
7. W. S. Kurth, D. A. Gurnett, F. L. Scarf, R. L. Poynter, *Nature* **312**, 27 (1984).
8. D. A. Gurnett, W. S. Kurth, S. C. Allendorf, R. L. Poynter, *Science* **262**, 199 (1993).
9. D. A. Gurnett, W. S. Kurth, E. C. Stone, *Geophys. Res. Lett.* **30**, 10.1029/2003GL018514 (2003).
10. D. A. Gurnett, W. S. Kurth, *Adv. Space Sci.* **16**, 279 (1995).
11. W. S. Kurth, D. A. Gurnett, *J. Geophys. Res.* **108**, 10.1029/2003JA009860 (2003).
12. See supporting material on *Science* Online.
13. D. A. Gurnett, W. S. Kurth, I. H. Cairns, J. Mitchell, *AIP Conf. Proc.* **858**, 129 (2006).
14. L. F. Burlaga *et al.*, *Science* **309**, 2027 (2005).
15. A. C. Cummings *et al.*, American Geophysical Union, Fall Meeting 2005, abstract SH51A-1184 (2005).
16. F. B. McDonald *et al.*, *Nature* **426**, 48 (2003).
17. S. M. Krimigis *et al.*, *Nature* **426**, 45 (2003).
18. J. R. Jokipii, J. Giacalone, J. Kota, *Astrophys. J.* **611**, L141 (2004).
19. R. Ratkiewicz *et al.*, *Astron. Astrophys.* **335**, 363 (1998).
20. N. V. Pogorelov, T. Matsuda, *J. Geophys. Res.* **103**, 237 (1998).
21. N. V. Pogorelov, G. P. Zank, *Astrophys. J.* **636**, L161 (2006).
22. V. Izmodenov, D. Alexashov, A. Myasnikov, *Astron. Astrophys.* **437**, L35 (2005).

23. We thank the staff at NASA Ames Research Center for the use of the Columbia supercomputer.

Supporting Online Material

www.sciencemag.org/cgi/content/full/316/5826/875/DC1
SOM Text
Figs. S1 to S4
References

3 January 2007; accepted 27 March 2007
10.1126/science.1139480

Ultralow Friction of Carbonate Faults Caused by Thermal Decomposition

Raehee Han,[1]* Toshihiko Shimamoto,[2]† Takehiro Hirose,[2]‡ Jin-Han Ree,[1] Jun-ichi Ando[3]

High-velocity weakening of faults may drive fault motion during large earthquakes. Experiments on simulated faults in Carrara marble at slip rates up to 1.3 meters per second demonstrate that thermal decomposition of calcite due to frictional heating induces pronounced fault weakening with steady-state friction coefficients as low as 0.06. Decomposition produces particles of tens of nanometers in size, and the ultralow friction appears to be associated with the flash heating on an ultrafine decomposition product. Thus, thermal decomposition may be an important process for the dynamic weakening of faults.

The strength of seismogenic faults, which is frictional resistance to fault slip during earthquakes, has been a major subject of debate in fault mechanics for 30 years (*1*, *2*). Although the stress–heat flow paradox for the San Andreas fault (no heat-flow anomaly, contrary to the prediction from in situ stress measurement and laboratory data of rock friction) favors extremely low fault strength (*3*, *4*), reasons for the weakness have been unclear. Recent work has shown that the dynamic weakening of faults during seismic slip can be caused by mechanisms such as frictional melting (*5*–*9*), thermal pressurization (*10*–*13*), and silica-gel formation (*14*, *15*). Fault gouge was also shown to exhibit pronounced slip weakening at high slip rates (*16*), presumably because of flash heating (*13*). Some analyses have predicted that slip-weakening distance, over which the initial peak friction drops to steady-state dynamic friction (*8*, *12*), and fracture energy (*13*, *16*) are of the same order as those parameters that are determined seismologically, narrowing the gap between laboratory studies of fault mechanics and seismology. Modeling the generation of large earthquakes is now becoming possible on the basis of the measured mechanical and transport properties of fault zones. Moreover, the dynamic weakening of faults may explain the lack of heat-flow anomaly after earthquake events along the San Andreas fault.

Thermal decomposition of rock-forming minerals at high ambient temperature and pressure can dramatically lower the strength of rocks because of the buildup of pore fluid pressure and the associated reduction of effective normal stress, provided that the sample is effectively undrained (*17*). Even at shallow crustal levels with low ambient temperature, thermal decomposition may occur at an elevated temperature because of coseismic frictional heating along fault zones. We demonstrated that a carbonate fault can lose frictional strength almost completely because of the thermal decomposition of calcite caused by frictional heating during high-velocity friction experiments on Carrara marble at seismic slip rates.

Forty-two friction experiments were conducted on precut bare surfaces of a pair of solid cylindrical specimens of Carrara marble (~99% calcite) at room temperature and room humidity. The experiments were carried out at normal stresses of 1.1 to 13.4 MPa and at equivalent slip rates of 0.03 to 1.30 m s^{-1}, with a rotary-shear, high-velocity friction apparatus at Kyoto University (*18*). The diameter and length of the specimen were 21.8 to 24.8 mm and about 20 mm, respectively (*19*). Because there is a slip-rate gradient across the fault due to cylindrical specimen geometry, we use the term "equivalent slip rate" ("slip rate" or "velocity" hereafter) (*7*, *18*, *19*).

[1]Department of Earth and Environmental Sciences, Korea University, Seoul 136-701, South Korea. [2]Division of Earth and Planetary Sciences, Graduate School of Science, Kyoto University, Kyoto 606-8502, Japan. [3]Department of Earth and Planetary Systems Science, Hiroshima University, Higashi-Hiroshima 739-8526, Japan.

*To whom correspondence should be addressed. E-mail: rhhan@korea.ac.kr
†Present address: Department of Earth and Planetary Systems Science, Hiroshima University, Higashi-Hiroshima 734-8526, Japan.
‡Present address: Instituto Nazionale di Geofisica e Vulcanologia, 00143 Rome, Italy.

At different slip rates (Fig. 1A), the friction coefficient of the specimens decreased nearly exponentially from peak friction, μ_p, to nearly steady-state friction, μ_{ss} (*20*), with increasing displacement. The slip-weakening distance ranged from a few to several meters. The μ_{ss} decreased markedly from ~0.6 to a range of 0.04 to 0.11 with an increase in slip rate (Fig. 1B). A linear friction law holds for both peak and steady-state friction, yielding μ_p of 0.60 ± 0.01 and μ_{ss} of 0.06 ± 0.01 (Fig. 1C). This μ_p value is more or less typical for marble (0.4 to 0.8) from conventional slow slip-rate (<1 mm s^{-1}) experiments (*21*). But μ_{ss} at a high slip rate (1.1 to 1.2 m s^{-1}) was extremely low. In contrast, μ_{ss} values remained high (0.46 to 0.63) at slow slip rates (0.03 to 0.08 m s^{-1}).

Microstructural observations and electron probe microanalysis of deformed specimens were conducted on thin sections normal to the fault and parallel to the slip direction. We started experiments with precut surfaces of Carrara marble, but gouge zones formed very quickly on both sides of the slip surface, which nearly coincides with the precut surface (Fig. 2A). Samples were collected from the slip surface for observations with a field-emission scanning electron microscope (FE-SEM) and a transmission electron microscope (TEM) and for x-ray diffraction (XRD) analyses. Those analyses revealed that the gouge zone forms at a very early stage of displacement (<2 m), when the outer and inner zones of gouge consist of calcite and lime (CaO) and/or hydrated lime [$Ca(OH)_2$], respectively. In the host rock adjacent to the fault gouge, fracturing of calcite grains occurred, and the size of calcite fragments decreased toward the slip surface to become calcite gouge. Calcite thermally decomposes into lime and CO_2 gas at about 720 to 900°C (*22*, *23*), and the lime can be transformed to hydrated lime by absorbing moisture when it is exposed to the atmosphere. Thus, thermal decomposition of calcite occurred from a very early stage of slip.

Many fractures were present over a wide decomposition zone between the decomposition fronts (DFs) (Fig. 2A); those fractures must have increased permeability. The decomposed zone consisted of grainlike aggregates ranging from about 100 to a few hundred nanometers in diameter (Fig. 2B), but each aggregate was composed of ultrafine grains that were several to a few tens of nanometers in size (Fig. 2C and fig. S3). Calcite decomposition was confirmed in specimens at fast slip rates (>0.4 m s^{-1}), but no evidence of decomposition was present in a specimen deformed at a slow slip rate of 0.08 m s^{-1} (run number HVR522; compare XRD curves in Fig. 2D). We did not recognize glass or amorphous material in any of the specimens (fig. S3).

To determine the timing of decomposition with respect to the slip-weakening behavior, we measured the emission of CO_2 released from a deforming sample by using two solid electrolyte-type CO_2 sensors (*19*). Sensor 1 (without a filter) was set very close to the fault (about 30 mm

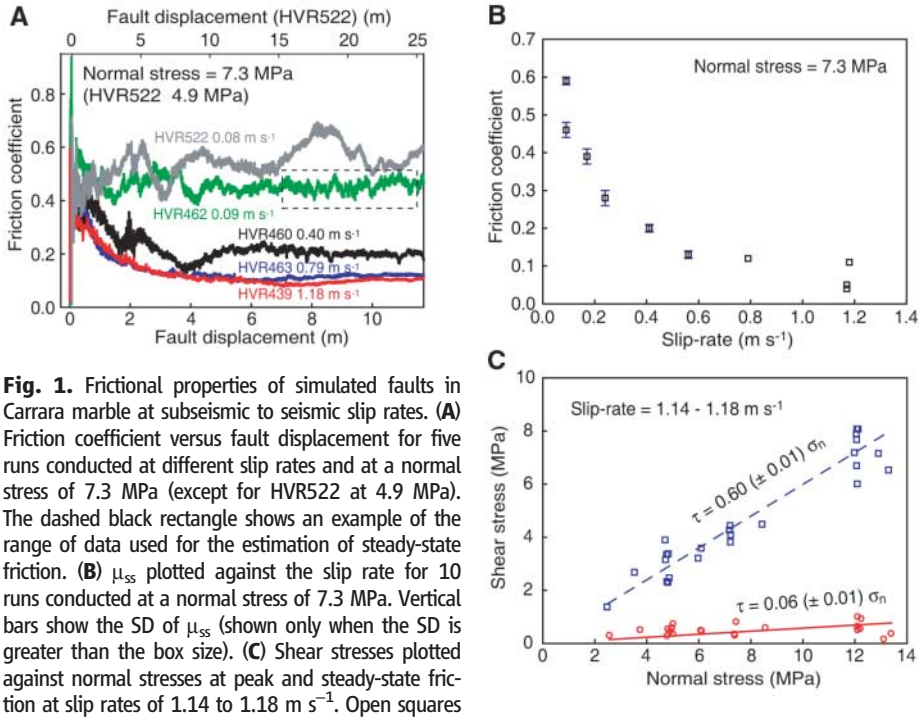

Fig. 1. Frictional properties of simulated faults in Carrara marble at subseismic to seismic slip rates. (**A**) Friction coefficient versus fault displacement for five runs conducted at different slip rates and at a normal stress of 7.3 MPa (except for HVR522 at 4.9 MPa). The dashed black rectangle shows an example of the range of data used for the estimation of steady-state friction. (**B**) μ_{ss} plotted against the slip rate for 10 runs conducted at a normal stress of 7.3 MPa. Vertical bars show the SD of μ_{ss} (shown only when the SD is greater than the box size). (**C**) Shear stresses plotted against normal stresses at peak and steady-state friction at slip rates of 1.14 to 1.18 m s^{-1}. Open squares and circles indicate initial peak friction and steady-state friction, respectively. The slopes of the lines give frictional coefficients at peak and steady-state friction. τ, shear stress; σ_n, normal stress.

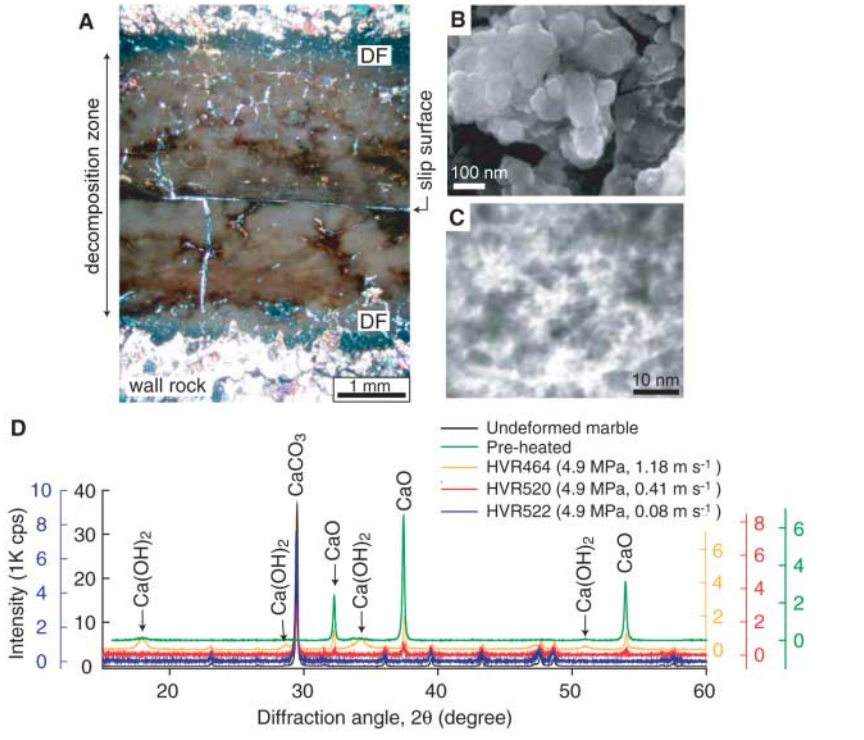

Fig. 2. Textures and decomposition products in fault zones. (**A**) A cross–polarized light photomicrograph of a thermally induced decomposition zone developed in Carrara marble, deformed at a slip rate of 1.30 m s^{-1} and at a normal stress of 4.6 MPa (HVR398, total slip = 125 m). DFs are between the wall rock and the decomposition zone. Slip was highly localized along the surface denoted by "slip surface." (**B** and **C**) SEM and TEM photomicrographs, respectively, illustrating microstructures of the lime (CaO) aggregates on the slip interface. (**D**) XRD spectra of an undeformed specimen, a preheated specimen, and specimens deformed at different conditions. Diffraction intensity is shown in 1000 × counts per second (cps) on all vertical axes.

away) to detect the onset of decomposition. It took about 0.9 to 1.0 s for this sensor to begin to detect CO_2. Sensor 2 (with a filter) had an initial response time of about 2 s and a 90% response time of ~90 s. This sensor was used to determine the total amount of CO_2 emission. At a high normal stress (12.2 MPa) and the largest slip rate (1.17 m s^{-1}), μ_p of about 0.6 dropped to μ_{ss} of about 0.04 (Fig. 3A). Sensor 2 showed a continuous increase toward a CO_2 concentration of about 29,000 parts per million. This concentration roughly agrees with the expected emission of CO_2 from the volume of decomposed calcite that was estimated on photomicrographs. The output from sensor 1 showed a reduction of CO_2 concentration after the end of a run because of dissipation of concentrated CO_2 near the fault (Fig. 3A). The first detectable output from sensor 1 was recognized at 1.0 s (Fig. 3B). The initial response time was 0.9 to 1.0 s for this sensor, so there must have been an emission of CO_2 almost immediately after the onset of slip (*24*). Another run at a lower slip rate (0.17 m s^{-1}) and at a normal stress of 9.8 MPa also indicated that the slip weakening was concurrent with the thermal decomposition of calcite (fig. S4).

Thus, a fault in Carrara marble clearly shows pronounced slip weakening at high slip rates while undergoing calcite decomposition along the slip surface. This means that a fault can become very weak as a result of frictional heating caused by its own motion. Such dynamic weakening should destabilize fault slip and foster the generation of large earthquakes (*13*). We next address the question of what causes such a pronounced weakening of a fault. One may consider that a buildup of pore pressure in a fault zone owing to the release of CO_2 gas is the most likely cause for fault weakening. To test this possibility, we conducted a critical experiment using preheated and decomposed specimens of Carrara marble (left in an oven at 900° to 904°C for 1.5 hours). We quantitatively confirmed complete decomposition by measuring weight loss after heating and by XRD analyses (Fig. 2D). The decomposed specimens could no longer emit CO_2 gas (*19*). The behavior is markedly similar between faults in Carrara marble and in decomposed specimens (Fig. 4). We have not measured the permeability of the decomposed zone in marble yet. But fractures in the decomposed zone in Fig. 2A suggest that the permeability of the decomposed zone is large enough for CO_2 to escape and to prevent the buildup of high pore fluid pressures. Enhanced permeability during the dehydration of serpentinite at elevated ambient temperature (not due to frictional heating) was also confirmed recently (*25*).

These results indicate that the weakening is attributed not to CO_2 pressure but to the low frictional strength of newly formed ultrafine lime grains. Among other possibilities, frictional melting can be immediately removed because calcite decomposition occurs before melting. Also, CaO melting would be unlikely because its melting temperature (~2572°C) is much higher than the temperatures recorded at the slip interface. Indeed, we did not detect any glass or amorphous materials in fault zones (fig. S3). Wrinkle-like pulses or normal separation of a fault along a bimaterial interface (*26*) is also unlikely because there is no material contrast across a fault in our experiments.

In view of the existing data, we considered that flash heating (*13*) at interfaces of ultrafine particles is critical for pronounced weakening of carbonate fault. The weakening by flash heating or transient local heating at asperity contacts has been proposed to occur via local melting at asperity contacts and/or by strength degradation of asperity contacts at submelting temperatures (*13*). The latter case is more likely for decomposed calcite because lime has a very high melting temperature. However, exact deformation mechanisms along sliding asperity or grain contacts still remain to be explored.

To demonstrate the importance of temperature rise during high-velocity sliding, we measured the temperature along the fault of the specimens (Fig. 3, C and D), using a radiation thermometer (*19*, *27*) during a run conducted at about the same sliding condition as that in HVR601. The thermometer measured an average temperature higher than 550°C over an area of 0.4 mm in diameter with a fast response time (<0.1 s). The measured temperature reached a maximum of 950°C at 30 s (high enough for calcite decomposition) after attaining about 650°C during the first 9 s (Fig. 3C). The local temperature at sliding asperities should be higher than the measured surface temperature even in the early stage (<9 s), in view of the CO_2 emission data (Fig. 3, A and B). The friction and thermal evolution in the final stages of the experiment are very interesting. After the specimen was disconnected from the motor, fault slip decelerated and stopped in about 3 s (Fig. 3, C and D). Friction increased at an accelerating rate as the temperature fell. The inverse relation between friction and temperature strongly suggests that the immediate strength recovery could be related to a rapid drop in temperature.

The simulated faults of Carrara marble exhibit lower friction than does the Nojima fault gouge, although their overall behaviors are similar (*16*). A possible reason for this difference is a very effective production of ultrafine grains that are tens of nanometers in diameter (Fig. 2C) by a

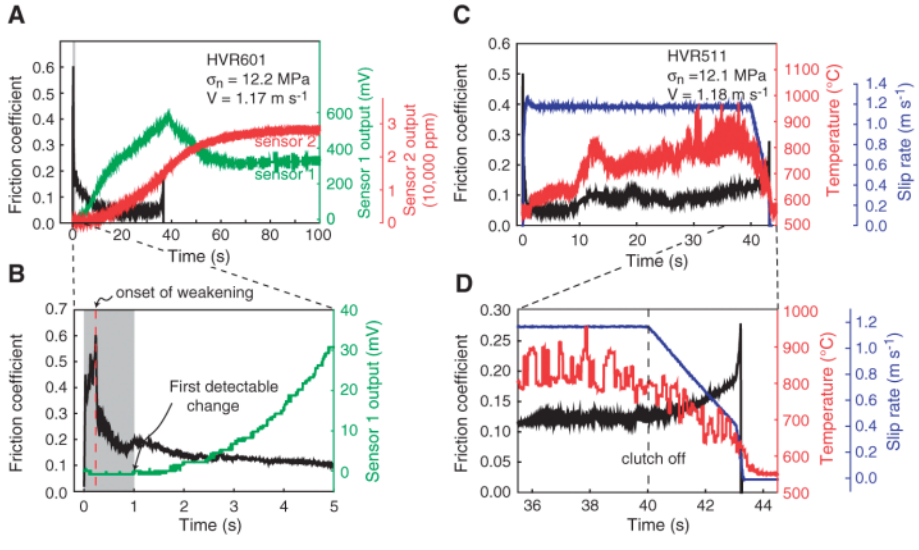

Fig. 3. Monitoring of CO_2 gas emission and temperature measurement. (**A**) Friction coefficient and outputs from two CO_2 sensors plotted against time. Sensor 1 (without a filter) is a quick-response sensor for detecting the onset of CO_2 emission, and sensor 2 (with a filter) is a slow-response sensor for monitoring the amount of emitted CO_2. *V*, slip rate. (**B**) Enlargement of (A) for the first 5 s of slip, with an output only from sensor 1 shown with mechanical data. The timing of peak friction and the first detectable change in output from sensor 1 are indicated by arrows. Vertical gray bars in both (A) and (B) indicate the response time of sensor 1 (about 1 s). (**C**) Friction coefficient (black), slip rate (blue), and temperature measured with a radiation thermometer (red) plotted against time in HVR511, which was conducted at about the same sliding condition (normal stress and slip rate of 12.1 MPa and 1.18 m s^{-1}, respectively) as that in HVR601. (**D**) Enlargement of the decreasing slip-rate phase of the experiment after turning off the magnetic clutch in (C).

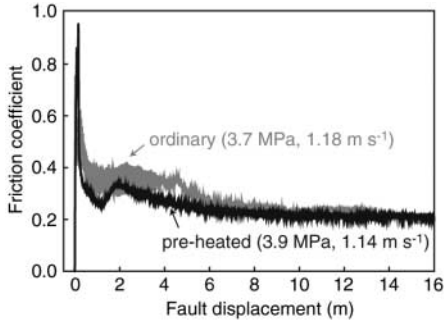

Fig. 4. Comparison of frictional behavior of a fault in Carrara marble (ordinary) and a fault in preheated and completely decomposed specimens of Carrara marble.

decomposition reaction (no time for grain growth during seismic-fault motion). The process may be similar to the cases of intermediate- to deep-focus earthquakes, for which the formation of ultrafine reaction products may play a decisive role in earthquake generation (*28*). Other gouge materials have to undergo grain comminution to form ultrafine grains, which requires extra work in fault zones, resulting in higher friction. For slip on faults in Carrara marble, understanding friction between nanometer-scale particles seems to be a key for delineating the exact mechanisms of the dynamic weakening of faults.

Our results have important implications for earthquake geology and fault mechanics. Marked decomposition weakening may be a widespread phenomenon, because fault gouges commonly contain sheet silicate minerals that decompose even at lower temperatures than that for calcite decomposition, although thermal decomposition of sheet silicates may be followed by frictional melting (*29*). Also, thermally induced decomposition may leave geological evidence (other than pseudotachylytes) of seismic-fault slip, contrary to geologists' opinion that faults do not preserve a record of seismic slip, except for the small percentage of faults containing pseudotachylyte (*30*). Indeed, we have shown that coseismic decomposition of siderite produces a stable mineral, magnetite (*31*). Thus, the clear demonstration of thermal decomposition during seismic slip opens up a new series of investigations in integrated fault and earthquake studies.

References and Notes

1. C. H. Scholz, *The Mechanics of Earthquakes and Faulting* (Cambridge Univ. Press, New York, ed. 2, 2002).
2. M. D. Zoback *et al.*, *Science* **238**, 1105 (1987).
3. J. N. Brune, T. L. Henyey, R. F. Roy, *J. Geophys. Res.* **74**, 3821 (1969).
4. A. H. Lachenbruch, J. H. Sass, *J. Geophys. Res.* **85**, 6185 (1980).
5. R. H. Sibson, *Geophys. J. R. Astron. Soc.* **43**, 775 (1975).
6. A. Tsutsumi, T. Shimamoto, *Geophys. Res. Lett.* **24**, 699 (1997).
7. T. Hirose, T. Shimamoto, *J. Geophys. Res.* **110**, B05202 (2005).
8. T. Hirose, T. Shimamoto, *Bull. Seismol. Soc. Am.* **95**, 1666 (2005).
9. G. Di Toro, T. Hirose, S. Nielsen, G. Pennacchioni, T. Shimamoto, *Science* **311**, 647 (2006).
10. R. H. Sibson, *Nat. Phys. Sci.* **243**, 66 (1973).
11. A. H. Lachenbruch, *J. Geophys. Res.* **85**, 6097 (1980).
12. C. A. J. Wibberley, T. Shimamoto, *Nature* **436**, 689 (2005).
13. J. R. Rice, *J. Geophys. Res.* **111**, B05311 (2006).
14. D. L. Goldsby, T. E. Tullis, *Geophys. Res. Lett.* **29**, 1844 (2002).
15. G. Di Toro, D. E. Goldsby, T. E. Tullis, *Nature* **427**, 436 (2004).
16. K. Mizoguchi, T. Hirose, T. Shimamoto, E. Fukuyama, *Geophys. Res. Lett.* **34**, L01308 (2007).
17. C. B. Raleigh, M. S. Paterson, *J. Geophys. Res.* **70**, 3965 (1965).
18. T. Shimamoto, A. Tsutsumi, *Struct. Geol.* **39**, 65 (1994) (in Japanese with English abstract).
19. Materials and methods are available as supporting material on *Science* Online.
20. μ_p is the ratio of the highest shear stress to normal stress before the onset of weakening, and μ_{ss} is the ratio of steady-state shear stress to normal stress.
21. M. S. Paterson, T.-f. Wong, *Experimental Rock Deformation—The Brittle Field* (Springer-Verlag, Berlin, ed. 2, 2005).
22. W. A. Deer, R. A. Howie, J. Zussman, *An Introduction to the Rock Forming Minerals* (Longman Scientific and Technical, Harlow, UK, ed. 2, 1992).
23. Z. D. Sharp, J. J. Papike, T. Durakiewicz, *Am. Mineral.* **88**, 87 (2003).
24. The calculated bulk temperature (~850°C) on the sliding surface after 0.2 s appears to be consistent with the immediate decomposition after the onset of slip (*19*).
25. E. Tenthorey, S. F. Cox, *Geology* **31**, 921 (2003).
26. D. J. Andrews, Y. Ben-Zion, *J. Geophys. Res.* **102**, 553 (1997).
27. A. Tsutsumi, T. Shimamoto, in *Contemporary Lithosphertic Motion in Seismic Geology: Proceedings of the 30th International Geological Congress*, Y. Hong, Ed. (VNU Science Press, Leiden, Netherlands, 1997), pp. 223–232.
28. H. W. Green II, C. Marone, in *Plastic Deformation of Minerals and Rock*, S. Karato, H.-R. Wenk, Eds. (Mineralogical Society of America, Washington, DC, 2002), pp. 181–199.
29. J.-H. Ree, R. Han, T. Shimamoto, J. Kim, *Eos* **87**, S33A (2006).
30. D. S. Cowan, *J. Struct. Geol.* **21**, 995 (1999).
31. R. Han, T. Shimamoto, T. Hirose, J.-H. Ree, J. Ando, *Eos* **87**, S33A (2006).

32. The observations of the experimental specimens were made with the use of TEM (JEOL JEM-2010) at the Natural Science Center for Basic Research and Development of Hiroshima University and FE-SEM (JEOL JSM-7000F) at Geodynamics Research Center of Ehime University. This work was supported by the Brain Korea 21 Project of the Ministry of Education, Korea Research Foundation grant C00435 (100699), the Grant-in-Aid for Scientific Research, Japan Society for Promotion of Science (16340129 and 18340159), and the Center of Excellence Program for the 21st Century of Kyoto University, "Active Geosphere Investigation."

Supporting Online Material

www.sciencemag.org/cgi/content/full/316/5826/878/DC1
Materials and Methods
Figs. S1 to S4
References

10 January 2007; accepted 26 March 2007
10.1126/science.1139763

GRACE Gravity Data Constrain Ancient Ice Geometries and Continental Dynamics over Laurentia

M. E. Tamisiea,[1]*† J. X. Mitrovica,[2] J. L. Davis[1]

The free-air gravity trend over Canada, derived from the Gravity Recovery and Climate Experiment (GRACE) satellite mission, robustly isolates the gravity signal associated with glacial isostatic adjustment (GIA) from the longer–time scale mantle convection process. This trend proves that the ancient Laurentian ice complex was composed of two large domes to the west and east of Hudson Bay, in accord with one of two classes of earlier reconstructions. Moreover, GIA models that reconcile the peak rates contribute ~25 to ~45% to the observed static gravity field, which represents an important boundary condition on the buoyancy of the continental tectosphere.

The similarity between the geometry of the free-air gravity anomaly (FAGA) over Laurentia (*1*) and the perimeter of the ancient ice complex that covered the region led to a long-held view that the perturbation largely reflected incomplete GIA in response to the ice age (*1–4*). In this case, the seismic high-velocity anomaly underlying the continent (*5*) would be interpreted as a neutrally buoyant, chemically distinct continental root, in accord with the tectosphere hypothesis (*6*). In contrast, forward analyses of GIA and/or mantle convection aimed at fitting the peak anomaly (*7–9*) have concluded that GIA is responsible for only ~10 to ~30% of the total signal. In this scenario, the seismic anomaly would be associated with active downwelling flow that drives a dynamic depression, and gravity low, on the overriding craton. Simons and Hager (*10*) have, on the basis of GIA modeling combined with an analysis of the spatio-spectral content of the Laurentian gravity field, proposed an intermediate scenario in which GIA and convection contribute roughly equally to the observed signal.

The characteristic time scale of GIA (a few thousand years) is orders of magnitude shorter than that of convective flow. Accordingly, Mitrovica and Peltier (*4*) suggested that consideration of the time rate of change of the gravity field would, when it became available, provide a robust method for isolating the GIA signal. The trend field would also provide finer spatial resolution of ice-sheet history than the static field. Observational constraints on gravity trends from land-based surveys in Hudson Bay exist (*11*, *12*), but these are too sparse to accurately constrain the regional (and peak) GIA signal. Recently, measurements obtained by the GRACE satellite mission (*13*) have reached sufficient time span to yield useful constraints on regional gravity trends. Our goal is to make use of the GRACE data to constrain the GIA signal and thus test the suite of published models for the dynamics of the Laurentian craton. We also use the GRACE-derived maps of gravity rates to address a century-long debate concerning the geometry of late Pleistocene ice cover over the region.

We use monthly Center for Space Research (CSR) RL01 GRACE solutions for the geoid,

[1]Harvard-Smithsonian Center for Astrophysics, 60 Garden Street, Mail Stop 42, Cambridge, MA 02143, USA. [2]Department of Physics, University of Toronto, 60 St. George Street, Toronto, ON M5S 1A7, Canada.

*Present address: Proudman Oceanographic Laboratory, 6 Brownlow Street, Liverpool L3 5DA, UK.

†To whom correspondence should be addressed. E-mail: mtamisiea@cfa.harvard.edu